Synchrotron Imaging of Keyhole Mode Multi-layer Laser Powder Bed Fusion Additive Manufacturing

*Yunhui Chen[1,2], Samuel J. Clark[1,2], Chu-Lun Alex Leung[1,2], Lorna Sinclair[1,2], Sebastian Marussi[1,2], Margie P. Olbinado[3], Elodie Boller[3], Alexander Rack[3], Iain Todd[4], *Peter D. Lee[1,2]

[1] UCL Mechanical Engineering, University College London, Torrington Place, London WC1E 7JE, UK

[2] Research Complex at Harwell, Rutherford Appleton Laboratory, Oxfordshire OX11 0FA, UK

[3] ESRF – The European Synchrotron, Grenoble, 38043 Cedex 9, France

[4] Department of Materials Science and Engineering, University of Sheffield, Sir Robert Hadfield Building, Mappin Street, Sheffield, S1 3JD, UK

Abstract

The keyhole mode in laser powder bed fusion (LPBF) additive manufacturing can be associated with excessive porosity and spatter, however, the underlying physics in multilayer build conditions remain unclear. Here, we used ultra-fast synchrotron X-ray imaging to reveal this phenomena. We revealed melt pool dynamics, keyhole porosity and spatter formation mechanisms and their impact in all layers of the build. We observed that the transient melt pool dynamics associated with the keyhole include: (I) keyhole initiation, (II) keyhole development, and (III) melt pool recovery. Porosity and spatter were associated with stages (II) and (III). We also discovered that droplet spatter can form due to the collapse of the keyhole recoil zone, causing molten particle agglomeration and ejection during stage (III). Our results clarify the transient dynamics behind the keyhole mode in a multi-layer LBPF process and can be used to guide the reduction in porosity and spatter in additive manufacturing. (150 words)

Keywords: Additive manufacturing, laser powder bed fusion; keyhole mode; synchrotron X-ray imaging

*Corresponding author: peter.lee@ucl.ac.uk, yunhui.chen@ucl.ac.uk

1. Introduction

Laser additive manufacturing (LAM), such as laser powder bed fusion (LPBF), is a key enabling technology that facilitates the fabrication of components with complex shapes directly from digital designs, layer by layer. LPBF is among the most promising methods in LAM due to its high accuracy[1]. The technique has been adopted in aerospace[2,3], biomedical[4,5] and energy storage[6,7] applications. However, the utilisation of LPBF for the manufacture of safety critical metallic components is hindered by technical challenges during processing which can lead to the formation of porosity, lack of fusion and cracking in the final part. Those features have a detrimental effect on the mechanical properties such as static strength, fracture toughness and resistance to failure by fatigue during cyclic loading. Porosity formation during melting and re-solidification of tracks in the powder bed, as successive layers are built, is one of the principal features that leads to reduced properties. In LPBF, the spatter, which is the ejection of particles from the melt pool during melting of powder materials, is a detrimental by-product which can contaminate the powder bed and/or adhere to the solidified track surface and increase the surface roughness. Both of these phenomena potentially increase the probability of porosity formation[8,9] in subsequent layer additions and so spatter formation[10] is a significant issue. It is therefore essential to gain an enhanced understanding of, and ability to prevent, porosity and spatter formation in order to realise the goal of industrialised production of safety critical LAM components.

Depending on laser energy density, a crucial indicator of energy input associated with laser power and scan speed, the laser-matter interaction may exhibit conduction mode or keyhole mode[11] melting during LPBF. If the energy input exceeds a certain criteria[12], LPBF is operated in keyhole mode when the power density of the laser beam is sufficient to generate metal evaporation. It is featured by a vapour cavity that enhances the laser absorption. The keyhole mode laser melting is frequently employed in LPBF as it allows the laser energy to transfer more efficiently to the powder layer by incorporating multiple reflections of the laser in the vapour cavity of the keyhole[13]. Consequently, the laser-matter interaction is very complex due to strong vaporisation of material from the molten pool and the flow of molten metal in the keyhole, driven by recoil pressure and Marangoni convection[14]. Whilst there are clear benefits to the use of keyhole mode conditions in LPBF, it often leads to excessive porosity[14] and spatter[15] if processing parameters are not properly controlled.

Therefore, it is critical to understand the mechanisms of porosity formation and spatter generation associated with the keyhole mode in order to optimise the integrity of components built by LPBF.

Recently, much research, including high speed imaging of the operation of LPBF, microstructural characterisation of built parts and computational modelling of the process has been performed to attempt to better understand keyhole and spatter phenomena[16,17]. In situ and operando high-speed X-ray radiography investigations have been proven to capture the transient phenomena in a range of processes, including LPBF[18,19]. Third-generation synchrotron radiation sources[20,21] enable high intensity X-rays to penetrate through a sufficient thickness of a metallic sample with ultra-high temporal (tenths of microseconds) and spatial (a few micro- metres) resolution. In LAM, synchrotron in situ research has focussed predominantly on single powder layer conditions in the experimental design to visualise the keyhole morphology[22] and the gas-liquid interface fluctuation[23] of the keyhole wall in a substrate plate. Additionally, pore circulation and elimination by thermocapillary force[24] and during hatching[25] has also been explored. A pore mitigation strategy was proposed to prevent pore formation by modulating laser power in keyhole mode with powder density of ~10.2 MW cm^{-2} [25]. While powder spatter is reported to be induced by the metal vapour jet/plume[26], laser absorption of powders and the role of powders and previous layers in multi-layer conditions were not addressed. Keyhole mode melt pool dynamics and its relation to both porosity and spatter formation mechanisms, especially in multi-layer conditions, are thus still unclear. Materials including stainless steel[10], bio-glass[19] and AlSi10Mg[24] have been explored in situ for their behaviour under laser irradiation. However, spatter formation in Ti-6Al-4V, which is a key material for aerospace and biomedical applications, has only been investigated in the bulk material.[27]

In the present work, we perform in situ and operando synchrotron X-ray radiography of LPBF in a five-layer build condition on a solid substrate, with 100 μm powder layer thickness on each layer. Our aim is to investigate the melt pool dynamics of the keyhole mode and its relationship with porosity and spatter formation mechanisms in Ti-6Al-4V. We reveal the melt pool dynamics which is a cyclic event with a transient separation of the portion of the melt pool in front of the laser. We elucidate how this cyclical process is related both to the generation of keyhole porosity and spatter formation in every layer of a build. The results presented in this work provide an enhanced understanding of LPBF AM which is directly relevant to multilayer powder bed printing of parts. The mechanisms observed are potentially applicable to other laser materials processing techniques such as directed energy deposition and laser welding.

2. Materials & Methods

2.1 *In situ* and operando synchrotron X-ray imaging

In situ and operando X-ray imaging on the ID19 beamline at the European Synchrotron Radiation Facility (ESRF) was performed to capture the melt pool and transient porosity and spatter dynamics in this study. The LAM process replicator, the In Situ and Operando Powder bed process Replicator (ISOPR), which mimics a commercial L-PBF system was developed so that it could be accommodated on the synchrotron beamline. The replicator comprises a laser and optical system, a powder bed with a vibration assisted gravity-fed powder hopper, a blade-type spreader and a processing chamber with an argon flow and Kapton X-ray windows. A 1070 nm Ytterbium-doped fibre laser (SPI Lasers Ltd, UK) of 200 W laser power (P) was selected for the laser system. It operates in a continuous-wave (CW) mode. It is equipped with f-theta lens to focus its spot size down to with a D4σ 50 μm with a symmetric Gaussian shape. The corresponding control system allows the scan speed (v) can reach 4 m s^{-1}. The actual scan speed was selected to enable a continuous track to be formed during laser melting. To adapt to X-ray imaging, a region of the powder bed 40 mm in width, 3 mm in height, and 0.3 mm in thickness were chosen (Supplementary Figure 1). It is positioned perpendicular to the X-ray beam and the laser beam (Fig. 1a). Two glassy carbon windows are fitted on the two sides of the CP-Ti substrate for complete transparency for the X-ray beam. Ti-6Al-4V powder (Supplementary Figure 2) is spread onto the substrate with hopper and the thickness is controlled with the motorised stage and blade spreader.

In this work, a commercially pure Ti substrate with dimensions of 46 mm in length and 0.3 mm in thickness in the x-ray direction was used as a substrate for the powder bed. The powder thickness of the first layer was controlled to be 100 μm and, after the melt-track was deposited the substrate was lowered by 100 μm and a new layer of powder was added. A schematic of the X-ray imaging process is shown in Figure 1a. Gas atomised Ti-6Al-4V powder was used in the experiments with a size range of 5 - 70 μm and a d_{50} *(median diameter)* of 45 μm (see Supplementary Figure 2). The powder bed is positioned inside the environmental build chamber which has X-ray windows and a flow of argon at 4 L min^{-1} is maintained throughout the experiment (see Supplementary). The scan speed was selected to be 100 mm s^{-1} to enable operating in keyhole mode with optimal imaging condition. In this operation condition, the laser powder density is 10.2 MW cm^{-2} which is above the threshold of ~0.4 MW cm^{-2} for keyhole mode operation[28].

A polychromatic beam was used for all trials with a peak X-ray energy of approximately 50 keV and a mean energy of approximately 30 keV. The X-ray imaging system consisted of a 200 μm thick LuAg: Ce scintillator and a 4× magnification long working distance objective lens (0.21 NA). The X-ray images was captured by a Photron FASTCAM SA-Z 2100K at 40 kfps. This configuration provided an imaging resolution of approximately 4.76 μm per pixel and an exposure time of 12.5 μs.

2.2 Image processing and quantification

We first apply a dark field correction in the Photron camera prior the image acquisition, and then we processed all the acquired radiographs using ImageJ[29] and Matlab©. The acquired images are further corrected to form a flat-field corrected (FFC) image by dividing by an average of 100 flat field images[19].

The melt pool was segmented using Otsu's threshold method[30]. And we used iterative PIV (Cross-correlation) plugin[31] from ImageJ to track the powder particles, melt flow and spatter (Details see Supplementary Figure 3). To increase the image contrast and signal-to-noise ratio, we applied a local-temporal background subtraction to reveal key information in the X-ray images following equation:

$$\mathrm{LTBS} = \frac{FFC}{I_{lavg}} \tag{1}$$

Where LTBS is the local-temporal background subtracted image, *FFC* is the flat field corrected image, and I_{lavg} is a local average of 50 of the nearest neighbour images (25 before and 25 after).

3. Results & Discussion

3.1 Evolution of a multi-layer melt track during LPBF on a substrate plate

We performed *in situ* and operando X-ray imaging on the ID19 - Micro-tomography beamline at ESRF to capture the transient phenomena during the LPBF of Ti-6Al-4V powder. The time-resolved evolution of the morphology of each melt track in a multi-layer series of melt tracks was captured by the X-ray imaging during laser melting and re-solidification (Fig. 1b and Supplementary Video 1).

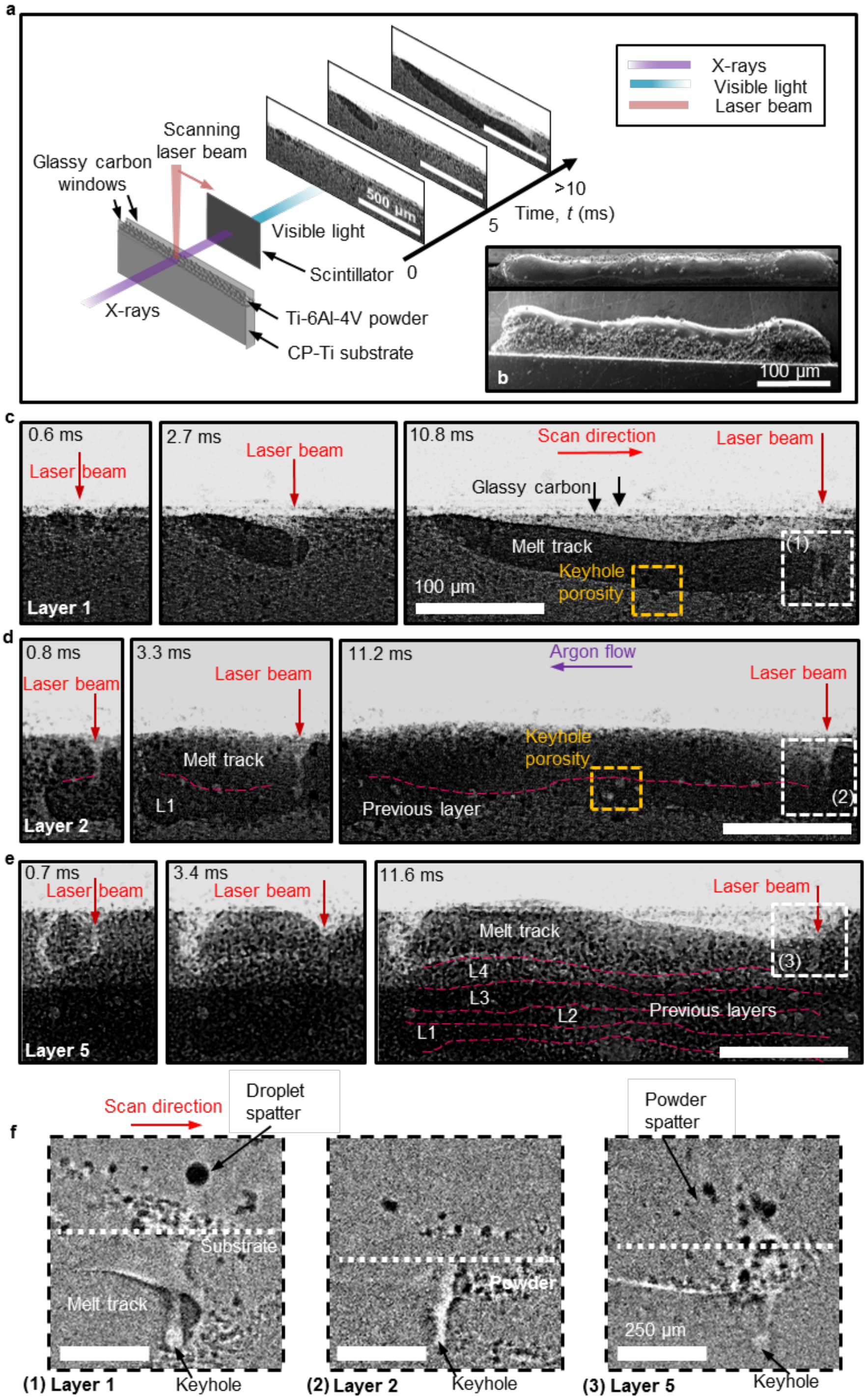

Figure 1. Evolution of a multi-layer melt track during LAM on a substrate plate. (a) Schematic of the *in situ* and operando X-ray imaging of LPBF AM of Ti-6Al-4V. Scale bar = 500 μm. (b) Corresponding SEM images (top view and side view) of the multi-layer melt track built during the in situ and operando experiment. Scale bar = 100 μm. (c)-(e) Time-series radiographs acquired during LAM of a Ti-6Al-4V 100 μm melt track under P =200 W, v = 100 mm s^{-1} during layer 1, layer 2 & layer 5 of the build, respectively. Three radiographs were chosen for each layer of the build to indicate the initial, middle and final stage of the build in each track and the time since the build started is marked on each radiograph. The melt tracks were deposited in an alternating directional strategy but the radiographs were reversed to keep the building directions uniform and are from left to right in the images. A significant number of keyhole pores are found at the interface between the deposited layers. See Supplementary Video 1. Scale bar = 100 μm. (f) Enlarged view of the vapour depression area (filtered using local-temporal background subtraction) in the dotted boxes in Figure 1(c), (d) and (e). The melt pool appears in projection to be separated into two portions: ahead of and behind the laser beam induced key-hole. Droplet and powder spatter are ejected by the metal/gas vapour jet from the denuded zone with an angle near normal to the substrate surface. Scale bar = 250 μm.

The melt tracks were deposited in an alternating directional strategy up to 5 layers in height. Figure 1c-e shows three images from the radiograph series taken from the start, middle and end of the deposition of the first, the second and the fifth layers, respectively (see Supplementary Video 1). The laser beam was seen to have consolidated powder particles into a continuous melt pool via laser melting and subsequent formation of a solidified melt track. The use of a thin substrate had a side-effect in the first layer of build. The melt pool touched the side wall, causing the surface of the melt-track to become depressed below the level of the original substrate. At the point of laser-matter interaction the laser is shown to have created a deep vapour depression, forming a keyhole throughout the melting process. Figure 1f provides an enlarged view of the vapour depression area in Figure 1c-e. We applied local-temporal background subtraction (details see methods section) to reveal the keyhole and spatter. Although one denuded (or powder free) zone surrounding the laser beam was reported previuosly[8] when observed from above, the radiographs showed that the melt pool is in fact separated into two portions: ahead of and behind the laser beam induced keyhole. This phenomenon was clearest in layer 1 as the image contrast between the melt pool and the substrate plate was better than with the powder in subsequent layers.

Most droplet and some powder spatter were ejected by the metal/gas vapour jet from the denuded zone (powder-free zone) with most of the droplet spatter ejected with an angle near normal to the substrate surface. We can distinguish whether spatter is droplet or powder by its diameter. Powder spatter had a diameter in the range of powder particles (~ 45 μm). Droplet spatter usually has a larger diameter (> 100 μm) which is a molten droplet formed from powder agglomeration. Of the powder spatter, some ejected normal, but some was observed to be ejected towards the melt track with a low angle.

Pores formed near the base of the keyhole and were apparently trapped by the fast-moving solidification front, preventing them from rising upwards or escaping through the surface of the melt pool via Marangoni convection. In this multi-layer build, the laser beam re-melted the previous layer whilst also consolidating powder particles in the track. A significant number of pores was found at the interface between the deposited layers (see Figure 1e – layer 5).

3.2 Keyhole melt dynamics and related spatter formation mechanism

A transient cyclic phenomenon of the keyhole melt pool dynamics was observed. (Figure 2 and Supplementary Video 2 & 3). We employed particle tracking to track powder particles movements and infer the fluid flow to elucidate melt pool dynamics and spatter formation. (Supplementary Figure 3) The dynamics of the keyhole melt pool can be defined as three stages. During Stage I, after a melt pool was formed at the start of the scan, the intense laser beam (power density of ~10 MW m^{-2}) separated the melt pool and created a vapour depression (keyhole). The narrow keyhole channel was known to be the result of the vaporisation of the alloy and the multiple reflections of the laser beam on the keyhole walls[13]. The superheated vapour expanded and caused a high-velocity jet of gas normal to the substrate surface (estimated up to 700 m s^{-1})[32] from the keyhole channel. Some of powder particles in the vicinity of the keyhole were ejected nearly normal to the substrate's surface with an average speed of 3 m s^{-1} as powder spatter (Supplementary Figure 4).

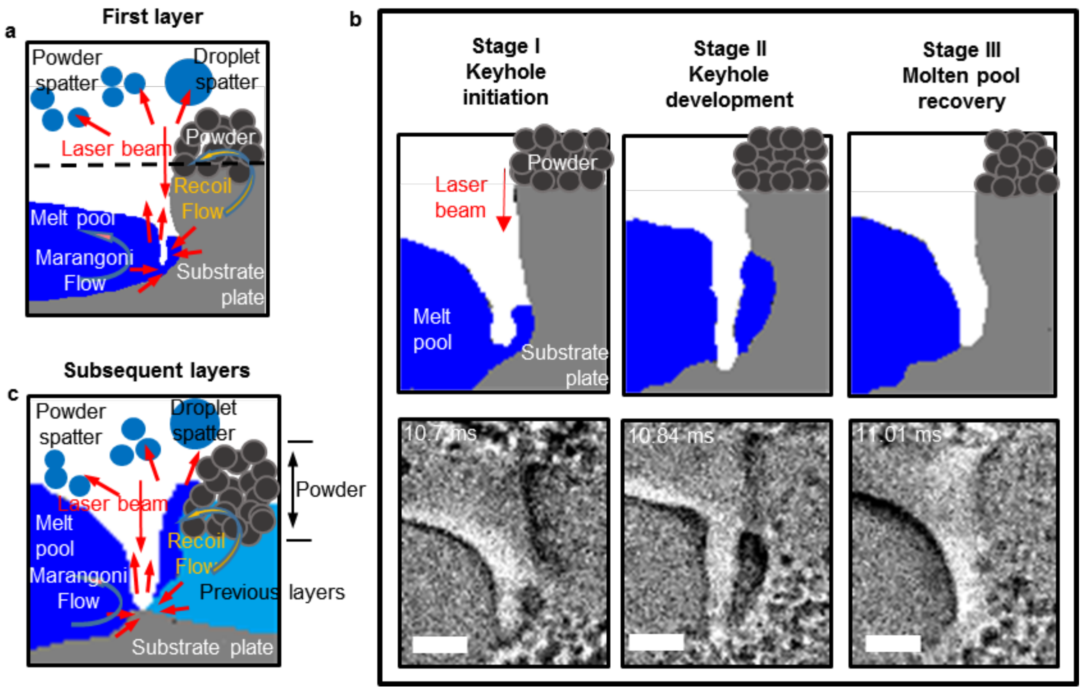

Figure 2. Melt pool dynamics revealed by X-ray imaging. (a) Schematics of the melt pool dynamics and spatter formation mechanisms in the first layer of build (See Supplementary Video 2). The melt pool is separated into two portions by the keyhole: ahead of and behind the laser beam. The Marangoni and recoil flow are contradictory and it caused a 'cut-off' of the melt flow underneath the vapour depression. Powder particles were being entrained into the melt-pool in the vicinity of the keyhole following the recoil flow and it formed molten droplets. Most droplet and some powder spatter are ejected by the metal/gas vapour jet from the denuded zone. (b) Schematics of the stages of the melt pool oscillation in the first layer. Three stages of melt pool dynamics were summarised as (I) Keyhole initiation, (II) Keyhole development, and (III) Molten pool recovery. The schematics were processed by image segmentation and the corresponding radiographs were revealed through local-temporal background subtraction. Scale bar = 100 μm. (c) Schematics of the melt pool dynamics in the subsequent layers (The phenomenon see Supplementary Video 3). The phenomenon is similar to the first layer of build. Due to the re-melting of the previous layer, there was no distinctly visible melt bead in front of the laser, however, the elongated front melt pool was still visible which is formed by vapour driven powder entrainment.

In stage II, the high-velocity intense vapour jet in Stage I caused a pressure decrease inside the keyhole[33]. As the high-velocity metal vapour jet propagated, it entrained argon gas and diverged. This induced a denudation zone[33] where powder particles were being entrained into the melt-pool in the vicinity of the keyhole following the recoil vapour flow and were engulfed into the front melt bead by capillary forces (see

Supplementary Video 2), creating a recoil flow. This is similar to the vapour-driven powder entrainment observations reported previously when building takes place on loose powder[34].

The Marangoni convection in the back portion of the melt pool is seen to be directed opposite to the building direction[32] and the recoil flow. As a result, it caused a temporary stall of the melt flow underneath the vapour depression and allowed the laser beam to vaporise this stagnant region and 'cut-off' the portion of the melt pool ahead of the laser (See Supplementary Video 2). Meanwhile, the melt bead in front of the laser increased the volume due to the entrainment of powder particles. During which, the powder particles on the top agglomerated by wetting and formed a molten droplet. These droplets were then entrained into the high temperature metal vapour and increased the pressure in the keyhole leading to Stage III. This is when the increase of keyhole pressure stabilized the keyhole and the front melt bead coalesced with the rear portion via wetting (See Supplementary Video 2). The melt pool recovery in the first layer was about *ca.* 1 ms after keyhole 'cut-off' in Stage II.

Overall, it is evident that the melt pool dynamics generated a perturbation of pressure in the vicinity of the keyhole, leading to changes in keyhole morphology and droplet spatter ejection (Figure 3). The mechanism is similar to that seen in the laser welding process described previously[35].

During Stage II of keyhole development in the first layer build, the projected keyhole was a narrow channel, as seen in Figure 2. The decrease of vapour pressure at this moment enabled the powder particles to agglomerate and to form droplet under recoil pressure without being ejected from the denudation zone (at 10.52 ms). During Stage III, Molten pool recovery, the keyhole opened up. Meanwhile, the vapour/gas jet with an increased pressure carried the droplet out of the keyhole with an angle near normal to the substrate surface (at 10.61 ms). The pressure in the keyhole then decreased before a new front melt pool is formed at Stage I(at 10.70 ms). We observed that the phenomena was more drastic with an increase of powder layer thickness. It indicated that an excess of powder particles was the main reason contributing to the pressure variation.

A similar cyclic phenomenon of the keyhole melt dynamics was also found in subsequent layers of the build (Supplementary Video 3). A vapour depression was formed on the previously built layer instead of the base plate after a melt pool was formed. Due to the re-melting of the previous layer, although the elongated front melt pool was still visible which was formed by vapour driven powder entrainment, the dynamic behaviour of the melt pool was not as clear as in the first layer. Similar to the first layer build, the vapour-driven powder entrainment enabled the front melt pool to increase its volume before it coalesced with the main melt pool. We observed that the melt pool separation phenomenon repeats periodically throughout the whole laser scanning process, revealing a new track formation mechanism (Supplementary Video 2) which is summarised, into three stages: (I) keyhole initiation, (II) keyhole development, and (III) molten pool recovery.

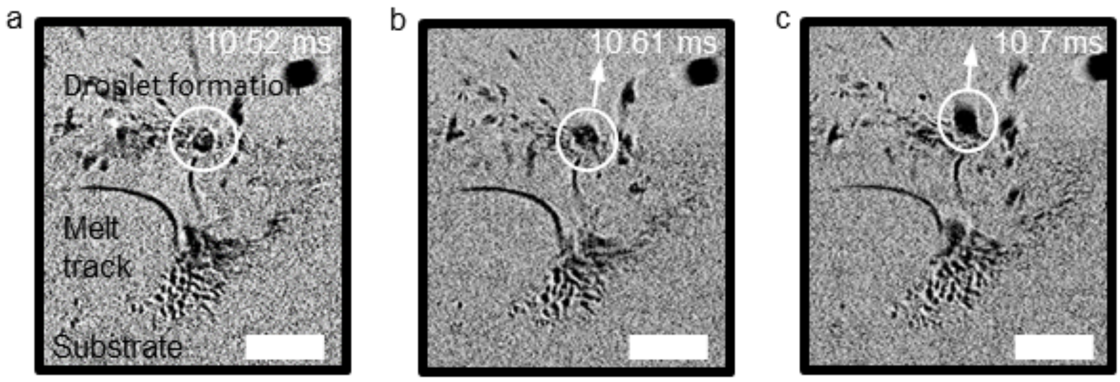

Figure 3. Time series of radiographs showing droplet spatter formation and its correlation with keyhole dynamics revealed through local-temporal background subtraction on the first layer of build. Three radiographs were chosen to indicate (a) droplet formation by molten powder agglomeration during Stage II Melt pool development, (b) droplet spatter ejection by the gas/vapour jet during Stage III Molten pool recovery, and (c) droplet spatter been ejected while the melt pool started another cycle and returned to Stage I Melt pool initiation. The time since the build started is marked on each radiograph. Scale bar = 250 μm.

3.3 Keyhole porosity formation mechanism

Keyhole porosity was observed to form during Stage II Melt pool development and Stage III Molten pool recovery. Abundant interlayer porosity was observed during the multi-layer build and pores are found to be introduced by the vapour depression. We employed particle tracking to reveal melt pool dynamics and spatter formation (Figure 4) when keyhole porosity was formed.

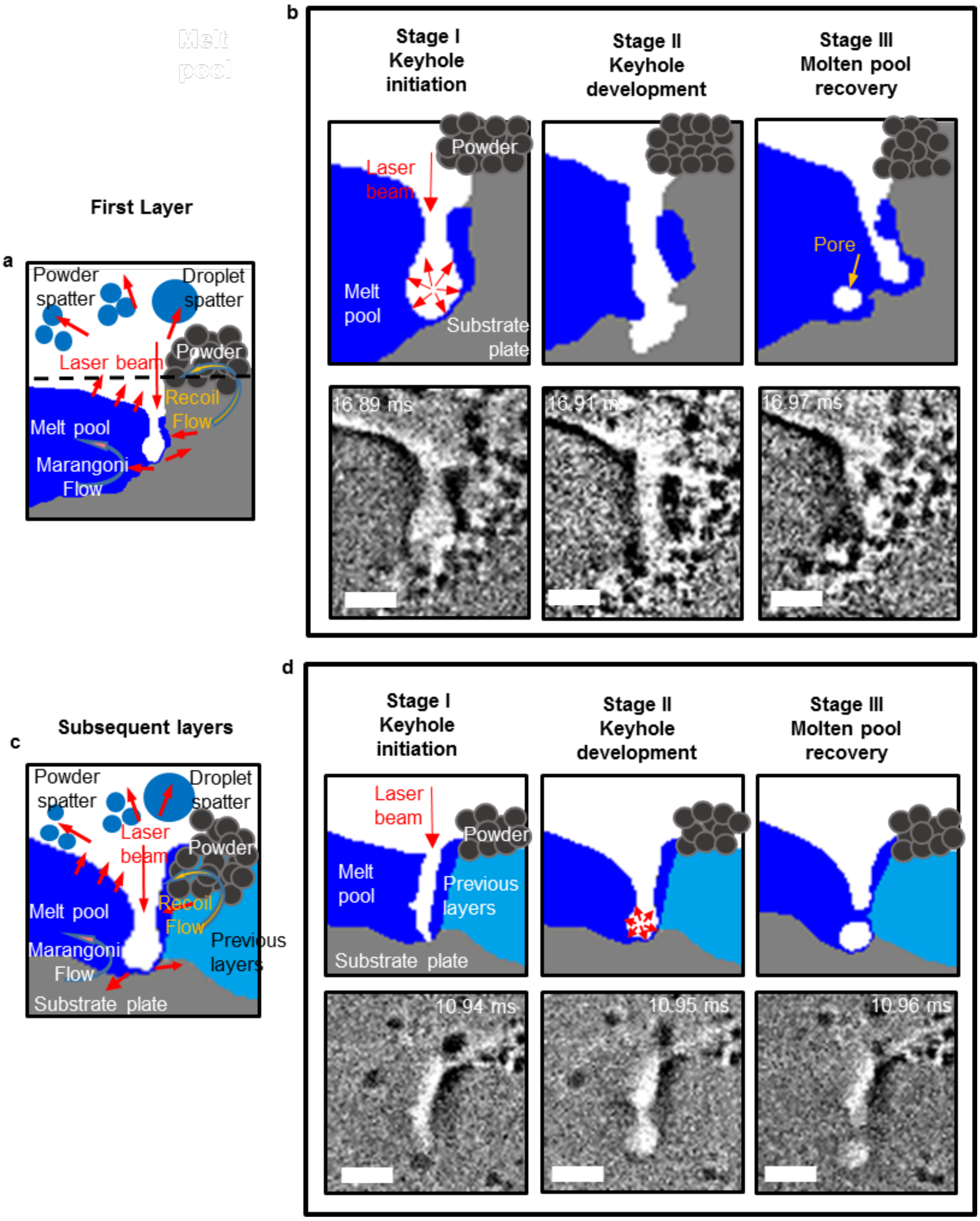

Figure 4. Keyhole porosity formation mechanism revealed by X-ray imaging. (a) Schematics of the phenomenon of keyhole pore formation in the first layer (See Supplementary Video 4). Similar to Figure 2(a), the melt pool was separated by the keyhole. The keyhole 'cut-off' was due to the rapid gas/vapour expansion inside the keyhole. Most droplet and some powder spatter are ejected by the metal/gas vapour jet from the denuded zone. (b) Schematics of the stages of the melt pool oscillation in the first layer. The three stages of melt pool dynamics are summarised as (I) Keyhole initiation, (II) Keyhole development, and (III) Molten pool recovery. The laser-induced gas/vapour was then entrained into the melt track below the keyhole and formed a keyhole pore. The schematics were processed by image segmentation and the corresponding radiographs were revealed through local-temporal background subtraction. Scale bar = 100 µm. (c) Schematics of keyhole pore formation phenomenon in the subsequent layers (See Supplementary Video 5). The phenomenon is similar to the first layer of build with a clear keyhole porosity formed in the melt track. (d) Schematics of the melt pool oscillation during keyhole pore formation in the subsequent layers. Three stages of melt pool dynamics were also summarised that matched with the first layer. Scale bar = 100 µm.

We hypothesise that in regions where the packing density[36] is locally reduced, more metal vapour is generated. This is due to a combination of the changes of surface contact area and the effective absorption and thermal conductivity from a looser powder layer. Lower packing density introduced higher local laser-powder interaction surface area, and it increased the local laser energy absorption, and thus increased the vaporization rate. We further hypothesise that when the powder packing density[36] varies along the laser scan path, more metal vapour was generated, compared to even powder packing density. Along with sufficient ambient argon gas, it caused a rapid gas/vapour expansion inside the keyhole during Stage I Keyhole initiation. The gas/vapour expansion rapidly pushed the molten liquid around it, causing a 'cut-off' of the melt pool as in Stage II Keyhole development. As the result, the laser-induced gas/vapour was then been entrained into the melt track below the keyhole and formed a keyhole pore during Stage III Molten pool recovery (Supplementary Video 4). Similarly, in the subsequent layers of build, the rapid gas/vapour expansion in Stage I created a 'cut-off' of the melt pool in Stage II. The gas/vapour was then been entrained beneath the keyhole during Stage III and formed a keyhole porosity (Supplementary Video 5).

3.4 Spatter formation mechanism correlated with keyhole porosity

The drastic cyclic oscillation of the melt pool generated a recoil pressure which promotes spatter to be ejected out of the denudation zone as shown in Figures 1, 2, 3 and 4. Some powder spatter was ejected at a low angle with respect to the substrate surface plane. Meanwhile, the stronger gas/vapour jet from Stage II during keyhole porosity formation enabled agglomerated molten droplets to be carried out nearly vertically at an average speed of 2.2 m s^{-1} as droplet spatter, as shown in Figure 5 and Supplementary Video 6.

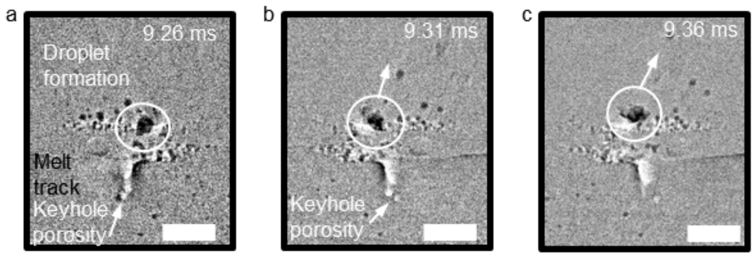

Figure 5. Time series of radiographs showing droplet spatter formation is associated with the cyclical melt pool dynamics and has a strong correlation with keyhole pore formation revealed through local-temporal background subtraction on the subsequent layer of the build. See Supplementary Video 6. Three radiographs were chosen to indicate (a) droplet formation by molten powder agglomeration during Stage II Melt pool development when a keyhole porosity was forming, (b) droplet spatter ejection by gas/vapour jet during Stage III Molten pool recovery when a keyhole porosity was formed, and (c) droplet spatter been ejected out while the melt pool started another cycle and back to Stage I Melt pool initiation. A keyhole porosity can be observed in the melt track. The time since the build started was marked on each radiograph. Scale bar = 250 μm.

The dominant formation mechanism for a molten droplet is the agglomeration of molten powder particles induced by the recoil pressure[37] during Stage II melt pool development. However, whether the molten droplet can be ejected as droplet spatter depends on the pressure of the vaporised gas flow from the keyhole. As we have observed, the agglomerated droplets can dissipate into the keyhole due to the lack of a sufficiently strong vapour jet when keyhole porosity did not occur. We also hypothesize that droplet spatter ejection is correlated with the formation of keyhole porosity during which a higher vapour pressure is generated. This phenomenon occurred in both the first layer and in the subsequent layers of the build.

Conclusions

We have used in situ and operando synchrotron X-ray imaging to uncover the key mechanisms of multi-layer LPBF of Ti-6Al-4V operating in keyhole mode. We revealed the underlying mechanisms of melt pool and keyhole dynamics and how this affected the mechanisms of porosity and spatter formation in multi-layer conditions. For the first time, we observed that melt pool separation and cyclic melt track evolution occurred during the building of 5 successive layers of Ti6Al4V. The melt pool oscillation involves three stages of evolution: (I) keyhole initiation, (II) keyhole development, and (III) melt pool recovery. We also elucidated both porosity and spatter formation mechanisms during the keyhole oscillation. Keyhole porosity was observed to form during the transient (I) keyhole initiation stage when the melt pool splits. Droplet spatter formation was directly correlated with the melt pool recovery stage by the agglomeration and subsequent ejection of powder particles introduced by recoil pressure in the denudation zone. The keyhole-related phenomena in a multilayer build were found to similar in all layers. Our results clarified the physics behind keyhole mode LPBF and can be coupled with modelling to improve the quality of LPBF built components. The mechanisms observed are applicable to more materials processing techniques such as laser welding and electron beam additive manufacturing where keyhole mode porosity and excessive spatter needed to be avoided.

Acknowledgement

The authors acknowledge financial support from MAPP: EPSRC Future Manufacturing Hub in Manufacture using Advanced Powder Processes (EP/P006566/1) and a Royal Academy of Engineering Chair in Emerging Technology, and Rolls-Royce plc. via the Horizon 2020 Clean Sky 2 WP5.8.1 programmes (YC) and through support of LS's studentship. We also acknowledge the use of facilities and support provided by the Research Complex at Harwell and thank the ESRF for providing the beam-time proposal (no: MA4061) and staff at ID19 beamline for technical assistance. The authors also thank Professor Graham McCartney for reading through the manuscript. We thank Photron ltd. for providing the high-speed camera (FASTCAM SAZ 2100K) to perform this experiment. We'd also acknowledge Dr. Samuel McDonald and Dr. Sam Tammas-Williams for their assistance during this beam time.

Author contribution

P.D.L. conceived the project. C.L.A.L. and S.M., led the design of the *In Situ and Operando* Powder bed process Replicator (ISOPR). C.L.A.L and Y.C. designed and performed the experiments, with all authors contributing. Y.C. performed the data analysis with S.C contributing. Y.C and P.D.L. led the results interpretation and paper writing, with all authors contributing.

References:

1. Tan Phuc, L. & Seita, M. A high-resolution and large field-of-view scanner for in-line characterization of powder bed defects during additive manufacturing. *Mater. Des.* **164**, 107562 (2019).

2. Wang, Y. *et al.* Probing deformation mechanisms of a FeCoCrNi high-entropy alloy at 293 and 77 K using in situ neutron diffraction. *Acta Mater.* **154**, 79–89 (2018).

3. Rometsch, P., Jia, Q., V. Yang, K. & Wu, X. Aluminum alloys for selective laser melting – towards improved performance. *Addit. Manuf. Aerosp. Ind.* 301–325 (2019). doi:10.1016/B978-0-12-814062-8.00016-9

4. Soro, N., Attar, H., Wu, X. & Dargusch, M. S. Investigation of the structure and mechanical properties of additively manufactured Ti-6Al-4V biomedical scaffolds designed with a Schwartz primitive unit-cell. *Mater. Sci. Eng. A* **745**, 195–202 (2019).

5. Nommeots-Nomm, A. *et al.* Four-dimensional imaging and quantification of viscous flow sintering within a 3D printed bioactive glass scaffold using synchrotron X-ray tomography. *Mater. Today Adv.* **2**, 100011 (2019).

6. Zhakeyev, A. *et al.* Additive Manufacturing: Unlocking the Evolution of Energy Materials. *Adv. Sci.* **4**, (2017).

7. Yufit, V. *et al.* Operando Visualization and Multi-scale Tomography Studies of Dendrite Formation and Dissolution in Zinc Batteries. *Joule* **3**, 485–502 (2019).

8. Matthews, M. J. *et al.* Denudation of metal powder layers in laser powder bed fusion processes. *Acta*

Mater. **114**, 33–42 (2016).

9. Choo, H. *et al.* Effect of laser power on defect, texture, and microstructure of a laser powder bed fusion processed 316L stainless steel. *Mater. Des.* **164**, 107534 (2019).

10. Guo, Q. *et al.* Transient dynamics of powder spattering in laser powder bed fusion additive manufacturing process revealed by in-situ high-speed high-energy x-ray imaging. *Acta Mater.* **151**, 169–180 (2018).

11. Rai, R., Elmer, J. W., Palmer, T. A. & Debroy, T. Heat transfer and fluid flow during keyhole mode laser welding of tantalum, Ti-6Al-4V, 304L stainless steel and vanadium. *J. Phys. D. Appl. Phys.* **40**, 5753–5766 (2007).

12. Fabbro, R. Scaling laws for the laser welding process in keyhole mode. *J. Mater. Process. Technol.* **264**, 346–351 (2019).

13. Dai, D. & Gu, D. Effect of metal vaporization behavior on keyhole-mode surface morphology of selective laser melted composites using different protective atmospheres. *Appl. Surf. Sci.* **355**, 310–319 (2015).

14. King, W. E. *et al.* Observation of keyhole-mode laser melting in laser powder-bed fusion additive manufacturing. *J. Mater. Process. Technol.* **214**, 2915–2925 (2014).

15. Liu, Y., Yang, Y., Mai, S., Wang, D. & Song, C. Investigation into spatter behavior during selective laser melting of AISI 316L stainless steel powder. *Mater. Des.* **87**, 797–806 (2015).

16. Everton, S. K., Hirsch, M., Stravroulakis, P., Leach, R. K. & Clare, A. T. Review of in-situ process monitoring and in-situ metrology for metal additive manufacturing. *Mater. Des.* **95**, 431–445 (2016).

17. Qiu, C. *et al.* On the role of melt flow into the surface structure and porosity development during selective laser melting. *Acta Mater.* **96**, 72–79 (2015).

18. Leung, C. L. A. *et al.* Laser-matter interactions in additive manufacturing of stainless steel SS316L and 13-93 bioactive glass revealed by in situ X-ray imaging. *Addit. Manuf.* **24**, 647–657 (2018).

19. Leung, C. L. A. *et al.* In situ X-ray imaging of defect and molten pool dynamics in laser additive manufacturing. *Nat. Commun.* **9**, 1–9 (2018).

20. Materlik, G., Rayment, T. & Stuart, D. I. Diamond Light Source: Status and perspectives. *Philos. Trans. R. Soc. A Math. Phys. Eng. Sci.* **373**, (2015).

21. Drakopoulos, M. *et al.* I12: The Joint Engineering, Environment and Processing (JEEP) beamline at Diamond Light Source. *J. Synchrotron Radiat.* **22**, 828–838 (2015).

22. Cunningham, R. *et al.* Keyhole threshold and morphology in laser melting revealed by ultrahigh-speed x-ray imaging. *Science (80-.).* **363**, 849–852 (2019).

23. Kouraytem, N. *et al.* Effect of Laser-Matter Interaction on Molten Pool Flow and Keyhole Dynamics. *Phys. Rev. Appl.* **11**, 1 (2019).

24. Hojjatzadeh, S. M. H. *et al.* Pore elimination mechanisms during 3D printing of metals. *Nat. Commun.* **10**, 1–8 (2019).

25. Martin, A. A. *et al.* Dynamics of pore formation during laser powder bed fusion additive manufacturing. *Nat. Commun.* **10**, 1–10 (2019).

26. Guo, Q. *et al.* Transient dynamics of powder spattering in laser powder bed fusion additive manufacturing process revealed by in-situ high-speed high-energy x-ray imaging. *Acta Mater.* **151**, 169–180 (2018).

27. Zhao, C. *et al.* Bulk-Explosion-Induced Metal Spattering During Laser Processing. *Phys. Rev. X* **9**, 21052 (2019).

28. Cunningham, R., Zhao, C., Parab, N. & Kantzos, C. Keyhole threshold and morphology in laser melting revealed by ultrahigh-speed x-ray imaging. **852**, 849–852 (2019).

29. Schindelin, J. *et al.* Fiji: an open-source platform for biological-image analysis. *Nat. Methods* **9**, 676–682 (2012).

30. Smith, P. *et al.* Otsu_1979_otsu_method. **C**, 62–66 (1979).

31. Tseng, Q. *et al.* Spatial organization of the extracellular matrix regulates cell-cell junction positioning. *Proc. Natl. Acad. Sci. U. S. A.* **109**, 1506–1511 (2012).

32. Bidare, P., Bitharas, I., Ward, R. M., Attallah, M. M. & Moore, A. J. Fluid and particle dynamics in laser powder bed fusion. *Acta Mater.* **142**, 107–120 (2018).

33. Matthews, M. J. *et al.* Denudation of metal powder layers in laser powder bed fusion processes. *Acta Mater.* **114**, 33–42 (2016).

34. Leung, C. L. A. *et al.* The effect of powder oxidation on defect formation in laser additive manufacturing. *Acta Mater.* (2018). doi:10.1016/J.ACTAMAT.2018.12.027

35. Ly, S., Rubenchik, A. M., Khairallah, S. A., Guss, G. & Matthews, M. J. Metal vapor micro-jet controls material redistribution in laser powder bed fusion additive manufacturing. *Sci. Rep.* **7**, 1–12 (2017).

36. Choi, J.-P. *et al.* Evaluation of Powder Layer Density for the Selective Laser Melting (SLM) Process. *Mater. Trans.* **58**, 294–297 (2017).

37. Khairallah, S. A., Anderson, A. T., Rubenchik, A. & King, W. E. Laser powder-bed fusion additive manufacturing: Physics of complex melt flow and formation mechanisms of pores, spatter, and denudation zones. *Acta Mater.* **108**, 36–45 (2016).